Research Square

Preprints are preliminary reports that have not undergone peer review.
They should not be considered conclusive, used to inform clinical practice,
or referenced by the media as validated information.

Towards Spatially Mapping the Degradation of Aluminium Anodes: A Group Theoretic Approach

Mikael Christodoulides

mikael.christodoulides@gmail.com

University of Cape Town https://orcid.org/0009-0001-6793-3513

Gerhard Venter

University of Cape Town https://orcid.org/0000-0003-3993-1198

Thorsten Becker

University of Cape Town https://orcid.org/0000-0002-4089-3574

Research Article

Keywords: aluminium anodes, group theory, electrode degradation, molecular dynamics, modelling, electron backscatter diffraction, misorientation

Posted Date: November 25th, 2026

DOI: https://doi.org/10.21203/rs.3.rs-11855548/v1

License: This work is licensed under a Creative Commons Attribution 4.0 International License.
Read Full License

Additional Declarations: The authors declare no competing interests.

Towards Spatially Mapping the Degradation of Aluminium Anodes: A Group Theoretic Approach

Mikael D.T. Christodoulides[1*], Gerhard A. Venter[2], Thorsten H. Becker[1]

[1] Centre for Materials Engineering, University of Cape Town, Cape Town, South Africa

[2] Department of Chemistry, University of Cape Town, Cape Town, South Africa

*Corresponding author: chrmik001@myuct.ac.za

Abstract

Aluminium metal anodes undergo rapid degradation during the early stages of charge cycling, due to a ~95% volume expansion resulting from the insertion of lithium ions. To study the spatial arrangement of this degradation, a mathematical function is developed using a quotient space to map the orientations of aluminium unit cells to scalar values of disorder. This function is shown to measure the accumulated disorder in strained aluminium tensile samples, using electron backscatter diffraction maps as input. A monotonic association with plastic strain and approximately normal distributions of disorder are observed. A molecular dynamics simulation is then developed to model the volume expansion of aluminium anodes during lithiation, specifically the arrangement of aluminium atoms underneath a lithiated surface layer. Applying the function yields spatial maps showcasing the initiation and propagation of disorder through the anode during lithiation. Disorder appears to initiate at small pockets directly underneath the lithiated surface, which coalesce into a network by 20 at.% lithium and an amorphous sea by 34 at.%. From 34-50 at.% lithium, disorder propagates down through the bulk of the anode in large regions which grow as composition increases, incorporating adjacent low-disorder atoms. It is concluded that the function serves as a promising candidate proxy for spatially mapping damage in lithiated aluminium anodes. Future work investigating the effects of high-disorder regions on dislocation mobility and recrystallization would build on the findings of this study and improve understanding of the degradation mechanisms in lithium-ion aluminium metal anodes.

Keywords: aluminium anodes, group theory, electrode degradation, molecular dynamics, modelling, electron backscatter diffraction, misorientation

Nomenclature

O_h	:	achiral octahedral symmetry
O	:	chiral octahedral symmetry
$SO(3)$	:	special orthogonal group
$\vec{x}$	:	position (unit cell)
ϕ	:	orientation (unit cell)
ω	:	distortion
$N(p)$	:	kernel
G	:	grain (equivalence class)
χ	:	local distortion
x_q	:	neighbour of x in q
ϕ_G	:	average orientation of G
GD	:	global distortion
$\mathcal{A}_p$	:	aliens of p
λ	:	offset
α	:	offset scalar
$\mathcal{X}$	:	disorder
ε	:	strain

1 Introduction

Aluminium metal has long been considered an appealing candidate material for lithium-ion battery (LIB) anodes, owing to its low cost, high capacity, environmental safety and dendrite suppression ability [1-7]. Aluminium metal anodes, however, suffer from seemingly intrinsic and rapid degradation mechanisms during the early stages of cycling [1, 2, 4, 7-10]. These shortcomings, though not comprehensively understood, are most often attributed to the mechanical stresses induced by a significant volume increase that accompanies lithiation [1, 4, 7-9]. The insertion of Li^+ ions into α-Al causes a volume expansion of 90-100% as β-LiAl phases form, which contorts surrounding α-Al grains and leads to cracks and microstructural degradation [4, 7, 11]. Concurrent kinetic and chemical processes, such as the loss of Li ions into the electrode bulk and the formation of cracks in brittle LiAl and pores in α-Al phases after $\beta \rightarrow \alpha$ phase transformations, may contribute to the anode's degradation [4, 12-14]. However, that the volume expansion of an aluminium anode is a critical cause for early-stage cycling failure is well-founded in existing literature [1, 4, 7-10]. Several strategies have been proposed to improve cycling performance through the introduction of alloying elements such as silicon [6], electrode coatings [1] or specific electrolyte choices [2]. To improve the cycle life of pure Al metal anodes, however, existing strategies are mostly limited to optimizing Al foils for hardness [7] or circumventing $\alpha \rightarrow \beta \rightarrow \alpha$ phase transformations entirely [10].

Experimental studies of electrochemical reactions, both in-situ and ex-situ, are notoriously difficult and expensive [15-17], and previous works have shown the utility of using molecular

dynamics simulations to study these phenomena instead [18-20]. Engines like LAMMPS [21] provide the means to analyse the full atomic arrangement of electrodes, which has proven useful in several prior studies [18-20, 22, 23]. The limited scale, however, of molecular dynamics simulations requires that such studies are constructed in careful, simplified ways. For lithiation, the primary phenomenon of interest is the bulk insertion of Li atoms into an electrode. The electrode should be large enough to contain a defensible microstructure, and recrystallization, charging kinetics and electrolyte effects would ideally be included. The space and time constraints of molecular dynamics, however, require a fair amount of simplification to be made when modelling such systems.

To investigate damage in lithiated aluminium anodes, orientation-imaging techniques are uniquely well-suited, allowing for full spatial maps of disorder (i.e. variations in unit cell orientations) in the anode to be obtained [24]. As metallic materials undergo plastic strain, the introduction of geometrically necessary dislocations causes curvature in the lattice structure, which results in a direct decrease in the homogeneity of unit cell orientations within grains [25]. Voids and other imperfections also reduce orientation homogeneity in a similar way [26]. To this end, accumulated lattice disorder serves as a proxy for plastic strain in damaged metal samples [27]. As such, plastic strain may be imaged by observing changes in the relative orientations of unit cells [24]. Though previous studies note that orientation measurements do not fully capture certain failure modes in metals [28], a number of others overall support the idea that these techniques offer unique capabilities for studying damage evolution [24, 25, 29-32]. Several prior works have shown the potential of quantifying, for example, plastic deformation in metals as a function of the relative misorientation amongst unit cells [31, 32]. In particular, local distortion (i.e. misorientation amongst a unit cell and its neighbours) at grain boundaries, and global distortion (i.e. misorientation within grains or across the material as a whole) are commonly used to measure disorder, and thus as proxies of damage in metals [29, 31-33]. Global distortion values such as grain orientation spread (GOS) are often used as the primary measure, as some studies claim that typical measures of local distortion, including kernel average misorientation (KAM), depend too heavily on measurement parameters to form clear correlations with damage [28, 30].

In this study, group theory is used to formally define misorientation values amongst aluminium unit cells and develop a function which maps unit cells to overall scalars of disorder based on these values. While symmetry and its underlying mathematics are extensively-used tools in crystallographic and texture analyses [34, 35], using symmetry-reduced misorientations to measure damage in polycrystalline materials in a formal, mathematical way has been less extensively explored. This approach has the benefit of providing clarity in how disorder values are assigned, by making clear where measurement conditions and other sensitivities affect the definitions which compose the function. Furthermore, since the function is built in a mathematical space, it consists of general definitions which are not constrained to any single application. This function is used in conjunction with a molecular dynamics simulation to investigate the spatial extent of disorder in lithiated aluminium anodes, allowing for insight into how disorder spreads throughout aluminium anodes during lithiation. It is argued that with disorder as a proxy for

damage, this approach defines a means towards spatially mapping the degradation of aluminium metal anodes.

Throughout this study, damage refers to any process which degrades the crystal structure of a metal, including voids, plastic strain and volume expansion stresses. Disorder refers to the resulting variation amongst unit cell orientations that damage produces, and which can be imaged using electron backscatter diffraction (EBSD) maps or similar techniques. Finally, distortion refers to quantitative measures of disorder, used throughout the mathematics to define what it means for a crystal structure to have accumulated disorder. In this way, the function below is developed using measures of distortion to spatially map disorder, which serves as a proxy for damage in aluminium metal.

2 Methods

2.1 Mathematical background

2.1.1 *Fundamentals*

Point groups are mathematical groups of rotation matrices which leave unchanged a single point in space [35-37]. The symmetry operations of the FCC unit cells found in aluminium, equivalent to those of a cube or octahedron, form the achiral octahedral point group O_h [38]. By restricting these operations to those which are physically possible by unit cells (i.e. proper rotations), one produces the 24-element subgroup $O \subset O_h$, known as the chiral octahedral point group [38]. These symmetry operations encode the equivalent ways to represent the orientation of an FCC unit cell using rotation matrices.

The matrix group $SO(3)$ also has utility for modelling these cells, defined as

$$SO(3) = \{M \in \mathbb{R}^{3\times3} \mid M^T M = I_3, \det(M) = 1\} \qquad \text{(Defn. 1)}$$

i.e. the infinite set of all rotation matrices in 3D space. It, alone, is a sufficient tool to model the orientations of fully asymmetrical rigid bodies. To capture symmetry, however, the left quotient space $SO(3)/O$ combines the two groups above into a new mathematical structure [37]. In particular, the elements of $SO(3)/O$ are left cosets, 24-element sets of rotation matrices which are symmetrical under the operations of O. To define them another way, the elements of $SO(3)/O$ are the equivalence classes of the equivalence relation $\sim \in SO(3)^2$, defined as

$$g_1 \sim g_2 \Leftrightarrow \exists o \in O \; st. \; g_2 o = g_1 \qquad \text{(Defn. 2)}$$

Using the tools above, an α-Al FCC unit cell was represented as an ordered pair $(\vec{x}, \phi)$ with components position and orientation, where

$$\vec{x} \in \mathbb{N}^3, \phi \in SO(3)/O \qquad \text{(Defn. 3)}$$

For applications where unit cells are thought of as elements on a 2D plane (i.e. in EBSD maps, etc.), this definition would be altered to $\vec{x} \in \mathbb{N}^2$.

2.1.2 *Misorientation, kernels and grains*

The distortion between unit cells was defined as the magnitude of the rotation needed to move between their orientations. In this way, distortion was given by a map $\omega: (SO(3)/O)^2 \to \mathbb{R}$, where for orientations ϕ_p, ϕ_q

$$\omega(\phi_p, \phi_q) = \min\left\{\arccos\left(\frac{Tr(x^{-1}y)-1}{2}\right) : x \in \phi_p, y \in \phi_q\right\} \qquad \text{(Defn. 4)}$$

The output of $\arccos$, and thus ω, is in degrees for the purposes of this definition and those which follow. It should also be noted that the elements which make up this set, i.e. when ignoring symmetry, are the "geodesic distances" between rotation matrices [39]. Geodesic distance is a metric [39], and in a similar way, given a set of orientations $\mathcal{O}$, it may be proven that $(\mathcal{O}, \omega)$ is a metric space and thus induces a topology. Though not directly applicable to aluminium anode degradation, proofs for both facts are given in **Appendix A**, and provide the potential for a richer mathematical space to be developed from the above.

The kernel of a unit cell p was defined as the set $N(p)$ of unit cells adjacent to it, i.e.

$$N(p) = \left\{q : 0 < \left|\vec{x}_p - \vec{x}_q\right| \leq \sqrt{3}\right\} \qquad \text{(Defn. 5)}$$

where q is a unit cell with position $\vec{x}_q$. If unit cells had 2D positions (i.e. $\vec{x} \in \mathbb{N}^2$), distance would be limited by $\sqrt{2}$. It should be noted that this quantity is affected by measurement conditions such as step size in applications using EBSD maps. This is a lesser concern for simulations, where all unit cells within a sample are considered. Furthermore, this definition allows one to define grains as the equivalence classes of the equivalence relation $\sim_G$, where for unit cells p, q,

$$p \sim_G q \Leftrightarrow \text{there is a chain } p = p_0, p_1, \dots, p_n = q \qquad \text{(Defn. 6)}$$

with $n \geq 0$ such that for $i < n$, $p_{i+1} \in N(p_i)$ and $\omega(\phi_{p_i}, \phi_{p_{i+1}}) \leq 5°$. For simplicity, the equivalence classes of $\sim_G$ were denoted with $G_1, G_2,$ etc. or simply G if only one was needed. Proofs that the concepts above were well-defined are given in **Appendix A** where needed, as for all subsequent definitions. It should lastly be noted that in applications where grains are defined using built-in methods, such as in MTEX or OVITO, the need for **Definition 6** is circumvented but the surrounding mathematics may still be applied. Since all unit cells belong to some grain by **Definition 6**, for software that imposes size limits on grains, unindexed pixels are mathematically equivalent to unit cells for which the grain is a singleton.

2.1.3 *Measures of distortion*

To define a mapping from $SO(3)/O$ to scalar measures of disorder, definitions for the local distortion amongst a unit cell and its neighbours (e.g. KAM), as well as the global distortion across the entire sample (e.g. average GOS) are required. Local distortion was the simpler of these definitions and was given by a map $\chi: \left(\mathbb{N}^3, \frac{SO(3)}{O}\right) \to \mathbb{R}$ where

$$\chi(p) = \frac{1}{|N(p)|}\sum_{q \in N(p)} \omega(\phi_p, \phi_q) \qquad \text{(Defn. 7)}$$

To define global distortion, the concept of an average orientation was required. To define this, we considered some grain G and some fixed matrix $x \in \phi_p$ for some unit cell $p \in G$. Given another unit cell $q \in G$, the neighbour of x in q was defined as the matrix $x_q \in \phi_q$ that corresponded to the minimal distortion to p, i.e. such that

$$\arccos\left(\frac{Tr(x^{-1}x_q)-1}{2}\right) = \omega(\phi_p, \phi_q) \qquad \text{(Defn. 8)}$$

Thereafter, the average orientation ϕ_G of a grain G was defined by taking an arbitrary fixed matrix $x \in \phi_p$ for some $p \in G$ and obtaining the coordinate-wise average of all the neighbours of x in G, i.e.

$$\overline{x} = \frac{1}{|G|}\sum_{q \in G} x_q \qquad \text{(Eq. 1)}$$

Then, the singular value decomposition of $\overline{x} = U\Sigma V^*$ gave $x_G = Udiag(1,1,\det(UV^*))V^*$ which defined the average orientation as

$$\phi_G = x_G O \qquad \text{(Defn. 9)}$$

With this defined, we noted that any set of unit cells will correspond to a set of grains $\mathcal{G}$, since $\sim_G$ is an equivalence relation and thus partitions the set. Therefore, the global distortion GD of a set of grains $\mathcal{G}$ was given by

$$GD = \frac{\sum_{G \in \mathcal{G}} \sum_{p \in G} \omega(\phi_G, \phi_p)}{\sum_{G \in \mathcal{G}} |G|} + 1 \qquad \text{(Defn. 10)}$$

The definition for GD above, excluding the $+1$ term, is equivalent to commonly-used definitions for GOS, such as in MTEX, averaged over the entire sample weighted by grain size.

2.1.4 *Offsetting grain boundaries*

What was last required was the offsetting of inflated values of χ across grain boundaries. While common approaches such as KAM often simply exclude unit cells in different grains, an alternative approach was to compute the component of χ contributed by these unit cells, and subtract this quantity multiplied by some scalar. This allowed for one to vary the extent to which these inflated values are offset, which is useful if inter-grain distortion values need to be preserved. We defined, for a given unit cell p, the set of unit cells in the kernel of p but a different grain as the aliens of p. These unit cells make up a set $\mathcal{A}_p$ where

$$\mathcal{A}_p = \{x \in N(p) : x \notin G\} = N(p) \backslash G \qquad \text{(Defn. 11)}$$

Then, the component of local distortion contributed by $\mathcal{A}_p$ was given by the offset λ: $(\mathbb{N}^3, \frac{SO(3)}{O}) \to \mathbb{R}$ where

$$\lambda(p) = \alpha\left(\frac{-|\mathcal{A}_p| \sum_{q \in N(p) \cap G} \omega(\phi_p, \phi_q)}{|N(p)||N(p) \cap G|} + \frac{\sum_{q \in \mathcal{A}_p} \omega(\phi_p, \phi_q)}{|N(p)|}\right) \qquad \text{(Defn. 12)}$$

if $\mathcal{A}_p \neq \emptyset$, or $\lambda(p) = 0$ otherwise. The scalar $\alpha \in [0, 1]$ should be assumed 1 unless otherwise stated.

2.1.5 *The disorder map*

Finally, the concepts above were combined into an overarching mathematical function of disorder in aluminium. Given a set of unit cells, the disorder at a unit cell p was given by the map $\mathcal{X}: \left(\mathbb{N}^3, \frac{SO(3)}{O}\right) \to \mathbb{R}$ where

$$\mathcal{X}(p) = \log_{10}\Big(\big(\chi(p) - \lambda(p)\big) \cdot GD + 1\Big) \qquad \text{(Defn. 13)}$$

This function was constructed under a few main considerations. It was logarithmic to allow for visualization of disorder on scales where both high and slightly-elevated regions of disorder occur. (In previous, non-logarithmic iterations, low-disorder regions were indistinguishable from undamaged regions in samples which had high disorder elsewhere.) Local distortion was the primary indicator of disorder at a unit cell, though scaled by a global distortion constant. Since GD is constant across a single map, its utility is only showcased when comparing the results between two maps, wherein the map with more disorder will have higher values of $\mathcal{X}$ as a result of the larger scalar. Lastly, 1 was added as a constant to ensure the map was well defined under the logarithm, since local distortion values of or near 0 are possible, and should result in a disorder value of zero rather than falling down the negative slope of the logarithm.

The final form of $\mathcal{X}$ is effectively a scaled KAM-GOS map, with formal definitions for symmetry-reduced misorientation. It is argued that defining the function in a mathematical space, however, has two unique benefits not apparent in standard definitions of these quantities. First, it is clear how all quantities which make up $\mathcal{X}$ are defined. With applications that introduce uncertainty, such as that resulting from measurement conditions, one may identify the particular quantities which are affected, e.g. $N(p)$, and interpret the results of $\mathcal{X}$ accordingly. Second, that $\mathcal{X}$ is defined using mathematics allows for it to be applied to any orientation-based data set, including but not limited to EBSD maps, simulations and ideal crystal structures. It is argued that this breadth of utility justifies the use of mathematics to formally define the quantities, such as KAM and GOS, which make up $\mathcal{X}$.

2.2 Tensile tests

To determine whether $\mathcal{X}$ served as a possible proxy for damage in aluminium, a tensile experiment was developed. Since tensile tests allow for a controlled extent of damage to be induced in a material [40], results from these tests provide confidence in how well the disorder map, $\mathcal{X}$, is able to act as a proxy for damage in aluminium. Rolled aluminium 1200 ($\geq$ 99% Al) ingots (Hulamin, South Africa) measuring $215 \times 28 \times 5\ mm^3$ were machined, as received, into four tensile test samples. Tensile samples were designed in accordance with the ASTM E8/E8M standard for metallic tensile tests [41], with $30 \times 10 \times 3\ mm^3$ clamping areas, a $32 \times 6 \times 3\ mm^3$ gauge region and a $6\ mm$ radius above the ends of the gauge region. Uniaxial tensile tests were

performed at room temperature according to ASTM E8/E8M on a universal testing machine equipped with a 10 kN load cell (Zwick 1494, Germany) at a crosshead speed of 1 mm/min. An initial tensile test was performed to failure on one sample to obtain the stress-strain curve shown in **Figure 1**. The 0.2% proof stress was found to be 36 MPa at 0.25% strain, and the ultimate tensile stress (UTS) was found to be 69 MPa at 21% strain. The remaining samples were strained to ~20% and ~40% of the way to ε_{UTS}, which for $\varepsilon_{yield} \approx 0$ could be expressed as

$$\frac{\varepsilon}{\varepsilon_{UTS}} \in \{0.2, 0.4\} \quad \text{(Eq. 2)}$$

as in **Table 1**, halting loading at a strain-controlled automatic trigger. In addition, a fourth sample of unstrained aluminium was used as an undamaged reference.

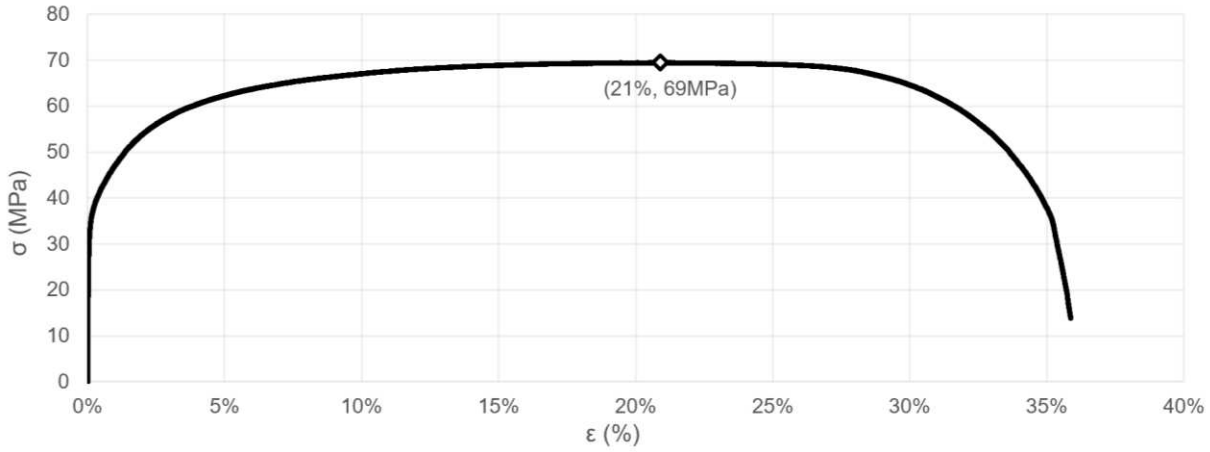

Figure 1: *Stress-strain curve for aluminium tensile samples, obtained from sample T4, with the ultimate tensile strength marked by ◇.*

2.3 Sample preparation and EBSD

Samples were cut to $10 \times 5\ mm^2$ and mounted in PP Black Aka-Resin (Akasel, Denmark) at 180 °C for 14 min (7 min hot, 7 min cooling) using a LaboPress-3 (Struers, Denmark) under 20 kN of force. Mounted samples were manually ground with 1200, followed by 2400 grit paper, and polished using Dia-Duo 2 3 μm solution (Struers, Denmark). Samples were then oxidatively polished using OP-S solution (Struers, Denmark), and ion-mill polished for 2×5 min runs at an accelerating voltage of 10 kV using an EM TIC 3X (Leica Microsystems, Germany). The unstrained aluminium sample T1 was electrochemically etched at 25V for 30 sec, and imaged using a Primotech Optical Microscope (Carl Zeiss Microscopy, South Africa) to obtain the material's grain size, which mostly ranged from 50-200 μm. EBSD maps for the three samples (excluding sample T4) were obtained using a MIRA™ 3 SEM (Tescan, Czech Republic) equipped with a Symmetry® S3 EBSD Detector (Oxford Instruments, England). EBSD maps were acquired using AZtec (Oxford Instruments, England) at an exposure time of 15 ms and step size of 1 μm, under an accelerating voltage of 20 kV and over a 450 μm map on a 600 μm view field. EBSD

maps were processed in MATLAB (R2026a, MathWorks, USA) using MTEX (v7.0.0) [42], with grains defined automatically using the built-in *calcGrains* method with a minimum size of 5 pixels and a 5° angle threshold. GD, χ and λ were implemented in the script as defined in **Section 2.1**, though for GD this was achieved using the built-in *grains.GOS* method. The entire codebase, for this and all other simulation and analysis scripts, is available online (see **Data Access**).

Table 1*: Strain values for the four aluminium tensile samples.*

Sample No.	$\boldsymbol{\varepsilon}$ (%)	$\frac{\boldsymbol{\varepsilon}}{\boldsymbol{\varepsilon_{UTS}}}$ (%)
T1	0	0
T2	4.24	20
T3	8.48	40
T4	Failure	-

2.4 Lithiation simulation

To model the volume expansion effects of lithium insertion into aluminium, a LAMMPS (22 July 2025, Sandia National Laboratories, USA) [21] simulation was developed with the PyLammps interface of the lammps module in Python (v3.12, Python Software Foundation, USA). A $300 \times 300 \times 60$ Å^3 polycrystalline aluminium slab consisting of 325255 atoms was instantiated using Atomsk (v0.13.1, Université de Lille, France) [43], with nine random Voronoi grains and a lattice parameter of 4.0493 Å. The slab was sectioned, using LAMMPS, into 3 layers as shown in **Figure 2**. The surface (~162k atoms), a 30 Å half of the slab and the site for lithium insertion, the core (~108k atoms), a 20 Å region underneath the surface and the region of study, and the base (~54k atoms), a 10 Å layer beneath the core fixed during molecular dynamics runs to provide a stable base for the layers above. The base was deemed necessary for simulating lithiation due to the atomic size constraints of the simulation, to ensure that stresses did not dissipate as a result of the anode's limited size. Aluminium and lithium potentials published by Roy et al. [44] were used with a modified embedded-atom method (MEAM), and the simulation was configured to use $s\ s\ m$ boundary rules (shrink-wrapped to allow for volume expansion), Brownian dynamics, a timestep of $1\ fs$ and a temperature of 300 K. Lateral faces were free to allow for in-plane expansion, though it should be noted that actual aluminium foil anodes are laterally constrained.

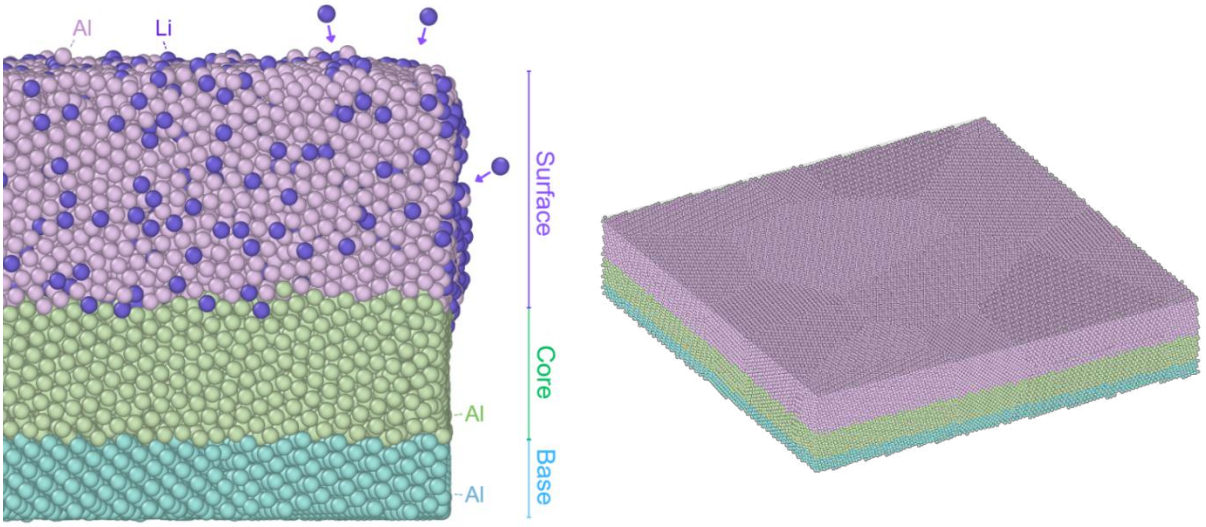

Figure 2: ***a)*** *The regions of the simulation where Li atoms are inserted (the surface), disorder values are computed (the core) and atom movement is fixed to prevent dissipation of volume expansion stresses (the base).* ***b)*** *The simulated aluminium anode geometry.*

Volume expansion was simulated by inserting Li atoms into the surface, as shown in **Figure 2**. Sites for Li insertion were chosen randomly from all atoms with potential energy values $\geq 0.15\ eV$ from the minimum potential energy across the surface. Overall, 10 lithiation runs were performed, denoted L2-L11, to various $at.\%$ Li surface compositions, as well as an unlithiated reference denoted L1. The composition of a fully lithiated surface phase was taken as $50\ at.\%$ Li, the composition of the β-LiAl front itself [4]. For all runs, the initial structure was minimized to a maximum of 500 steps, using a conjugate gradient algorithm with an energy tolerance of $1 \times 10^{-5}\ eV$. These parameters were also used in all subsequent minimizations unless otherwise specified. Li atoms were inserted in bouts of 1000 at random positions within 6 Å wide spheres centred at random high-energy surface atoms. An insertion was aborted if no suitable sites, defined using an overlap threshold of 1.8 Å, could be found in 1000 iterations. The exact insertion sequence is stored with the output files in the code repository (see **Data Access**), including the random seeds used. The structure was then minimized as before, a short molecular dynamics run of 300 steps was performed, and the structure was minimized again, before the next bout of Li atoms was added. Note that the number of surface atoms fluctuated very slightly over runs L1-L11 due to atom migration across the surface-core interface, and high-energy surface atoms expelling from the anode mass which were removed in subsequent runs. This was accounted for in all composition calculations.

To simulate delithiation, a 12th run was performed to remove all Li atoms from the surface and revert to $0\ at.\%$ Li. During this run, denoted D, atoms were removed from the surface layer in bouts of 1000, from the bottom of the surface region (i.e. $z = 30$ Å) upwards. After each deletion, the structure was briefly annealed at 600K for 100 steps, then at 300K for 100 steps and then minimized up to 200 steps. Once all Li atoms had been removed and the delithiated structure was

obtained, a final, longer minimization up to 500 steps was performed, with an energy tolerance of $5 \times 10^{-5}\ eV$.

Table 2: *Simulation parameters for lithiation simulation runs.*

Run Number	Insertion/Deletion-Minimization Cycles	Li Atoms	Surface Region at. % Li
L1	0	0	0.00
L2	1	991	0.60
L3	2	1960	1.18
L4	3	2936	1.74
L5	6	5861	3.36
L6	12	11731	6.30
L7	17	16535	9.23
L8	42	41218	20.2
L9	83	82159	34.1
L10	123	122152	43.7
L11	158	157308	50.2
D	158	0	0.00

2.5 Postprocessing

The results from all simulation runs were processed in OVITO (v3.16.1 Basic, OVITO GmbH, Germany) [45] using polyhedral template matching (PTM) algorithm [46] with a root mean square deviation cutoff of 0.1 to define grains. Thereafter, grain segmentation was applied with a minimum grain size of 100 atoms using the graph clustering (automatic) algorithm, in replacement of **Definition 6**. Since PTM allows for orientation assignments to individual atoms based on their local environments, atoms resulting from simulation runs were treated as unit cells. Atomic positions, orientations and grain IDs of all core atoms were exported to text files, which were preprocessed in Python to match the format of **Definitions 1-13** (most notably from quaternions to matrices). Libraries numpy (v2.4.0) [47] and scipy (v1.18.1) [48] were used to determine values of ω. Kernels were defined using the CutOffNeighborFinder class of the ovito library using a cutoff shell of 5 Å, roughly equal to $\sqrt{3} \times 2.86$ Å, the interatomic distance of aluminium metal [49]. GD, χ, λ and $\mathcal{X}$ were all implemented in Python based on their definitions above. Results were exported to text files and processed using OVITO and Excel (v2611, Microsoft, USA).

3 Results

3.1 Tensile tests

Inverse pole figure (IPF) maps and heatmaps of disorder (i.e. $\mathcal{X}$) from each tensile sample's EBSD map are shown in **Figure 3**. Samples T1, T2, and T3 contained 18, 23, and 23 grains respectively, with grain sizes ranging from roughly 50-200 μm, and indexing rates for these

samples of 81%, 81%, and 71%. One grain in sample T1 was poorly indexed, though unindexed pixels were otherwise distributed arbitrarily across the surfaces, with no clear effect on disorder. Grain size and morphology varied both within and between the three EBSD maps.

Table 3: *Longitudinal strain, global distortion, average disorder, median disorder, standard deviation of disorder and the 5th-95th percentile range of disorder, for all tensile samples.*

Sample	ε_ℓ (%)	GD	$\overline{\mathcal{X}}$	$\widetilde{\mathcal{X}}$	$SD_{\mathcal{X}}$	$\widehat{\mathcal{X}}_{0.95} - \widehat{\mathcal{X}}_{0.05}$
T1	0	7.44	1.17	1.16	0.24	0.76
T2	4.24	7.35	1.41	1.40	0.22	0.71
T3	8.48	13.10	1.76	1.76	0.23	0.76

Results shown in **Table 3** show that disorder increased monotonically with strain from T1→T2→T3. Average disorder values increased by 0.24 and 0.35 from T1→T2 and T2→T3, respectively, with Cohen's d values of 1.08 and 1.55. This suggested that shifts in disorder against strain were large relative to the spread of each map. Increases in disorder from T1→T2→T3 furthermore presented as uniform across the surfaces, with no distinct high-disorder regions visible. Global distortion values correlated less clearly with strain, increasing from T2 to T3 but decreasing slightly from T1 to T2. Standard deviation values were around 0.2 across all populations, and ranges between the $5th$ and $95th$ percentiles were around 0.7. Median values of disorder for all samples sat very close to the average, suggesting that populations were symmetrical. All populations appeared approximately normally distributed, as shown in **Figure 3**, and exhibited overall similar shapes.

3.2 Lithiation simulation

Simulation runs L1-D produced ~1 million outputs of $\mathcal{X}$ across the core regions of all runs. Spatial maps of disorder were obtained using OVITO's visualization tools, with six of these maps shown in **Figure 4**. Surface atoms were automatically assigned null disorder values, and roughly half of all inflated grain-boundary disorder values were offset by λ, though atoms in grain boundaries ≥ 3 atoms thick showcased as high disorder due to OVITO's shared grain ID assignment for unindexed atoms. Spatial maps for the unlithiated ($0\ at.\%$ Li) and $0.6\ at.\%$ Li slabs showed an increase in disorder across the entire anode, with values in grains jumping from $\mathcal{X} \approx 0$ to ~1 and between grains from $\mathcal{X} \approx 2$ to ~2.5. No distinct high-disorder regions formed, with the increase in disorder presenting as roughly uniform across grains and grain boundaries. At $1.18\ at.\%$ Li, small pockets of disorder ($\mathcal{X} \approx 2.4$) 3-4 atoms large had begun to form within grains near the surface-core interface ($z = 30$ Å). The insertion of additional Li atoms formed more of these pockets, rather than growing those already existing. By $9\ at.\%$ Li, each grain contained a number of pockets (around 5-20, depending on size) though the underlying microstructure was still clearly visible.

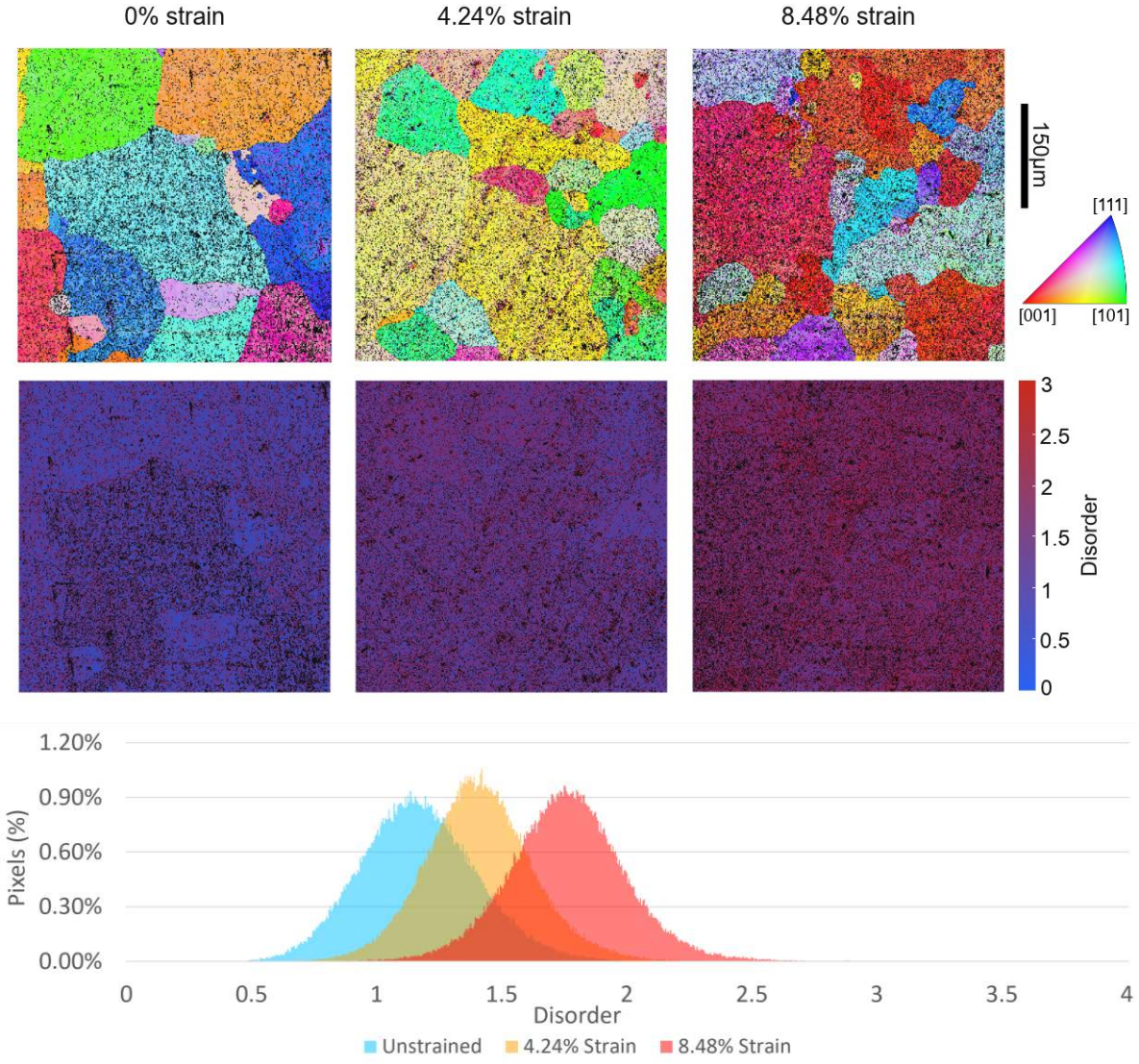

Figure 3: ***a)*** *IPF maps and disorder heatmaps for aluminium tensile samples.* ***b)*** *Frequency plots showing the distribution of disorder values for aluminium tensile samples.*

By 20 $at.\%$ Li, the microstructure near the interface has largely broken down, and pockets coalesced into a high-disorder ($\mathcal{X} \approx 2.5$) network spanning across the slab, shown at the bottom of **Figure 4**. At this composition, disorder was mainly localized at the interface, with evidence of the high-disorder network hidden below 10 Å from the interface. By 34 $at.\%$ Li, the network at the interface had transformed into an amorphous sea of high-disorder ($\mathcal{X} \approx 3$) atoms. Across the remaining thickness of the anode, high-disorder regions had begun to propagate down from the interface into the bulk of the anode, producing contrasting high-disorder ($\mathcal{X} \approx 3$) and low-disorder ($\mathcal{X} \approx 1.4$) zones. The interface sea remained relatively unchanged until 50 $at.\%$ Li, and appeared to be the state of maximum disorder within the anode. Overall, disorder values of high- and low-disorder regions did not change meaningfully between 34-50 $at.\%$ Li. That said, high-disorder

bulk regions continued propagating down the anode from 34-50 $at.\%$ Li, as well as growing horizontally by incorporating adjacent low-disorder atoms into themselves, leading to the shrinking of nearby low-disorder grains.

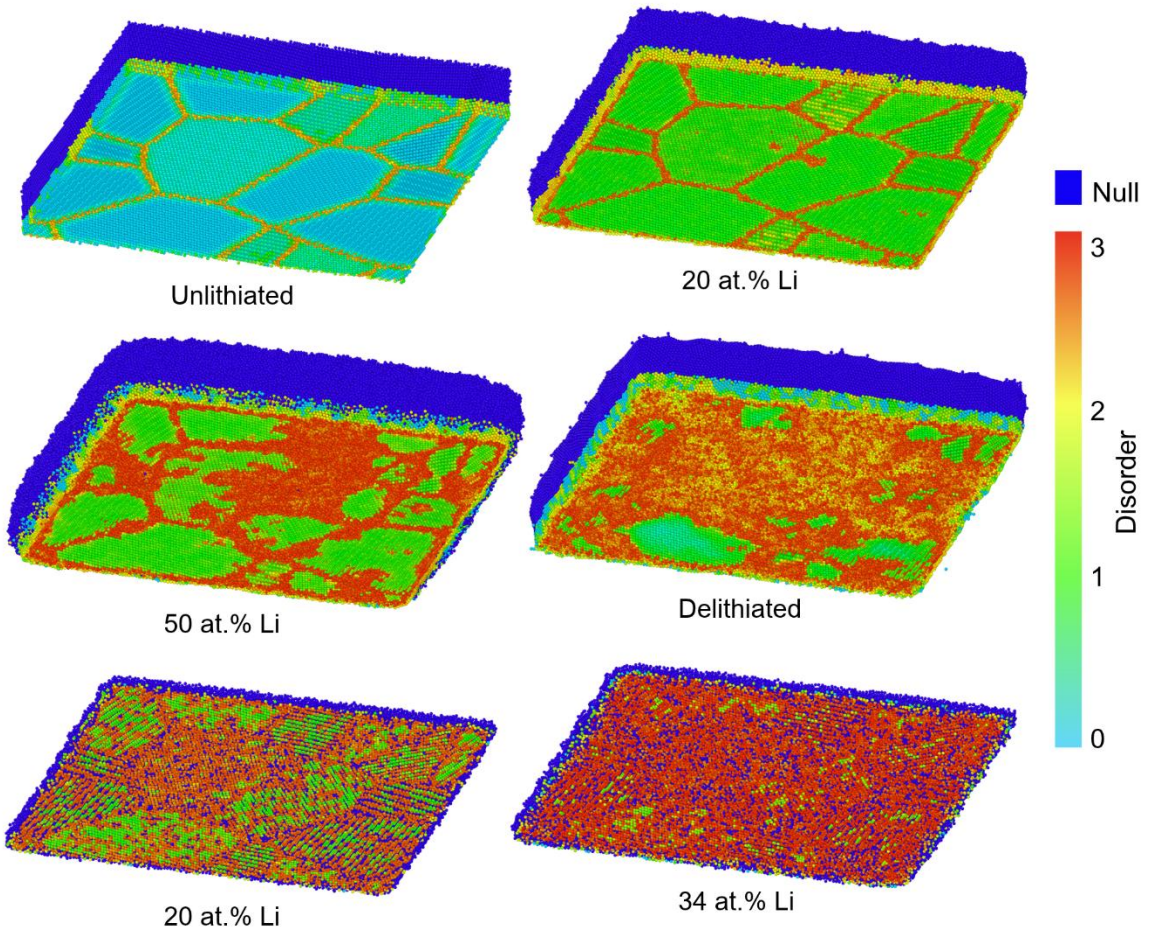

Figure 4: *OVITO figures showing the distribution of disorder values for core α-Al atoms sliced at z=18 Å (12 Å from the interface) for the top four and z=27 Å (showing the interface) for remaining two, at various lithium compositions.*

After delithiation, disorder values within previously high-disorder regions dropped substantially at the interface though the microstructure did not regenerate, as expected within the simulated timeframe. Average disorder values in the amorphous sea dropped substantially to around $\mathcal{X} \in [1.5, 2.25]$, ranging somewhat arbitrarily across the sea and not forming any distinct low or high-disorder regions. Disorder values in the bulk of the anode appeared more persistent than at the interface, and a gentle gradient was seen along the thickness of the anode from interface disorder values to the now higher-disorder bulk regions. Disorder values within the bulk were still contrasting between high-disorder regions and unincorporated grains, though high-disorder

regions coalesced into a connected, amorphous zone as a result of the atomic movement facilitated by run D. Due to this, the microstructure was overall less clear than at full lithiation, with only a few small low-disorder grains remaining. Disorder values ranged arbitrarily across this zone around $\mathcal{X} \in [2, 3]$, seemingly independent of the locations of previous high- and low-disorder regions at $50\ at.\%$ Li. Low-disorder grains still not incorporated into this zone remained relatively unchanged, though smaller, but displayed slight decreases in disorder for the atoms furthest from their borders.

Table 4: *Simulation results summary for all lithiation/delithiation runs.*

Run	Average Disorder	GD	Core Volume (nm^3)	Core Expansion (%)	Surface Volume (nm^3)	Surface Expansion (%)	Interface Expansion (%)
L1	0.536	5.93	1813	0.00	2723	0.00	0.00
L2	1.15	10.7	1867	3.01	3052	12.1	0.01
L3	1.34	9.97	1898	4.69	3092	13.5	0.35
L4	1.31	11.6	1902	4.94	3083	13.2	0.37
L5	1.35	10.7	1914	5.59	3163	16.1	0.70
L6	1.33	9.10	1916	5.68	3267	20.0	1.34
L7	1.35	9.33	1948	7.42	3308	21.4	1.45
L8	1.64	10.9	1966	8.46	3747	37.6	4.39
L9	1.97	15.9	2143	18.18	4510	65.6	9.85
L10	2.09	14.4	2184	20.49	5247	92.7	14.7
L11	2.13	14.6	2163	19.31	5870	115	17.8
D	2.20	13.6	1870	3.14	4264	56.6	4.77

Average values of disorder increased throughout lithiation, as seen in **Table 4**, showcasing an approximate linear correlation with $at.\%$ Li for runs L2-L11. This correlation was also observed between average disorder and percent interface expansion, as seen in **Figure 5**. Also shown in this figure is the trend between disorder and strain noted for the tensile tests, with strain computed as longitudinal for tensile samples and as a change in interface area for the lithiation runs. Disorder values for the unlithiated and delithiated samples, L1 and D, fell considerably below and above this trend line, respectively. Global distortion values did not show a clear trend, falling into three distinct buckets around 6, 10 and 15. An increase in average disorder was also observed between the $50\ at.\%$ Li and delithiated samples, though GD decreased slightly.

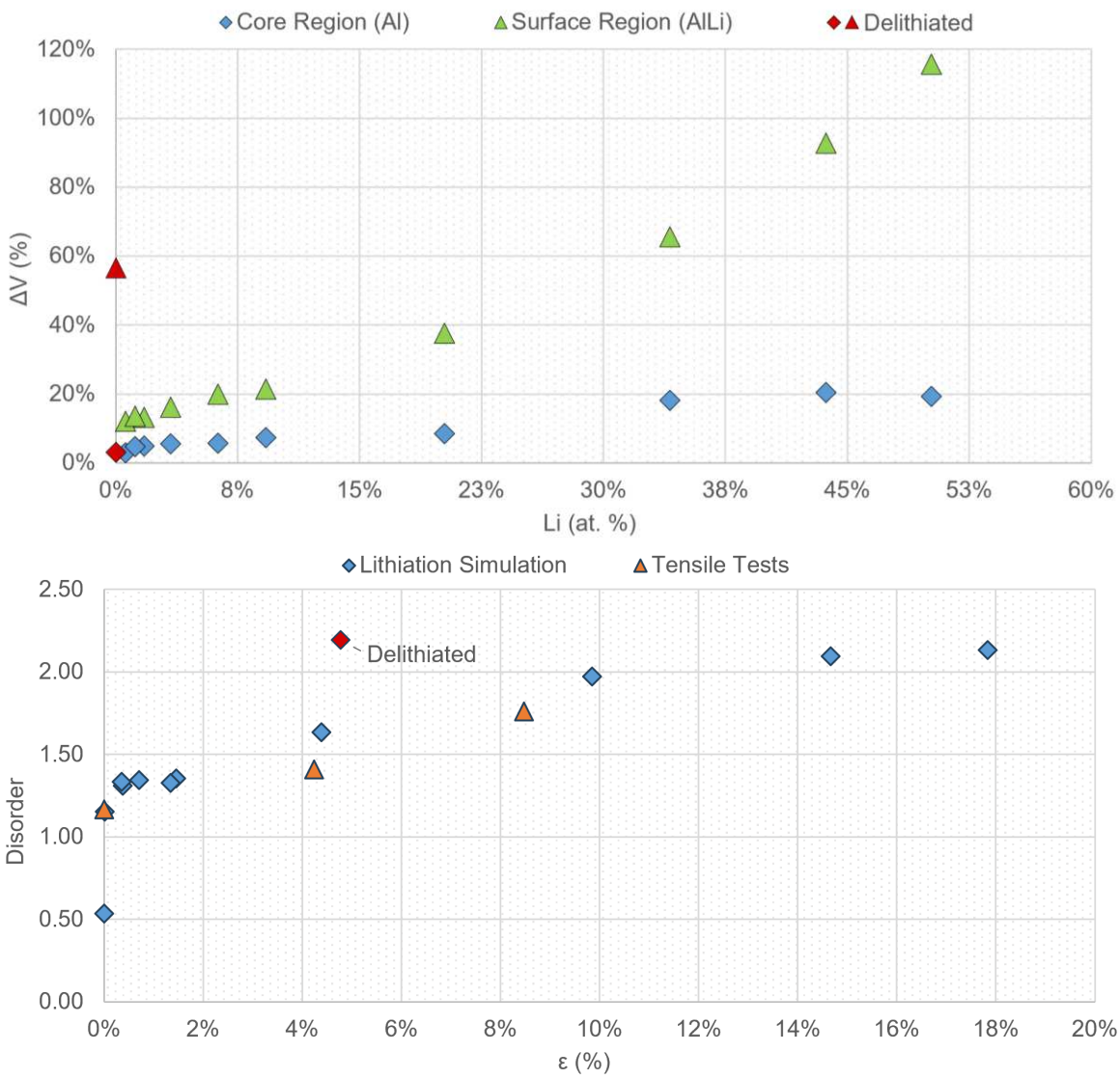

Figure 5: *Scatter plots showing a) volume change against surface at. % for both the core and surface regions b) disorder values against strain for core α-Al atoms and aluminium tensile samples.*

The volume of the core and surface regions prior to lithiation were their expected results of $\sim 1800\ nm^3$ and $\sim 2700\ nm^3$. By 50 $at.\%$ Li, the surface region had expanded by $\sim 115\%$, and remained expanded by 56.56% after delithiation, compared to the unlithiated sample. The core region showed a more modest expansion of 19.31% by 50 $at.\%$ Li, and interestingly a larger expansion of 20.49% at 44 $at.\%$ Li. After delithiation, the core region dropped to an expansion of 3.14%. The relationship between volume expansion and $at.\%$ Li appeared mostly monotonic for the core region, and convex for the surface, as in **Figure 5.**

Frequency distributions of disorder, shown in **Figure 6**, represent the relative proportions of disorder values at various lithiation stages. For the unlithiated sample, a small peak is visible at $\mathcal{X} \approx 2.3$ as a result of non-offset grain boundary disorder values, though most atoms otherwise sat

with disorder values very close to 0. Note the peak at $\mathcal{X} \approx 0$ is truncated in the figure below, and reached close to 3% in actuality. With the introduction of the first 1000 Li atoms, a bimodal distribution formed, with two distinct peaks at $\mathcal{X} \approx 0.7$ and $\mathcal{X} \approx 2.7$. These peaks were visible for the remainder of lithiation, but the right peak grew noticeably in size as high-disorder atoms increased in their proportion. By full lithiation (i.e. 50 $at.\%$ Li), the right peak had surpassed the left peak, despite being considerably smaller at the time of their formation. The left peak appeared to shrink to accommodate for this, but also shifted notably rightwards from 0.6-34 $at.\%$ Li, ending at $\mathcal{X} \approx 1.3$. A tail to the right of the left peak which was initially visible from ~1 to ~1.5, faded as this shift occurred. No visible shift occurred from 34-50 $at.\%$ Li, and no such shift was observed in the right peak. In the delithiated sample, much of the right peak remained, with a smaller hump to its left, though the left peak appeared to spread into a roughly flat distribution from ~0.3 to ~1.8.

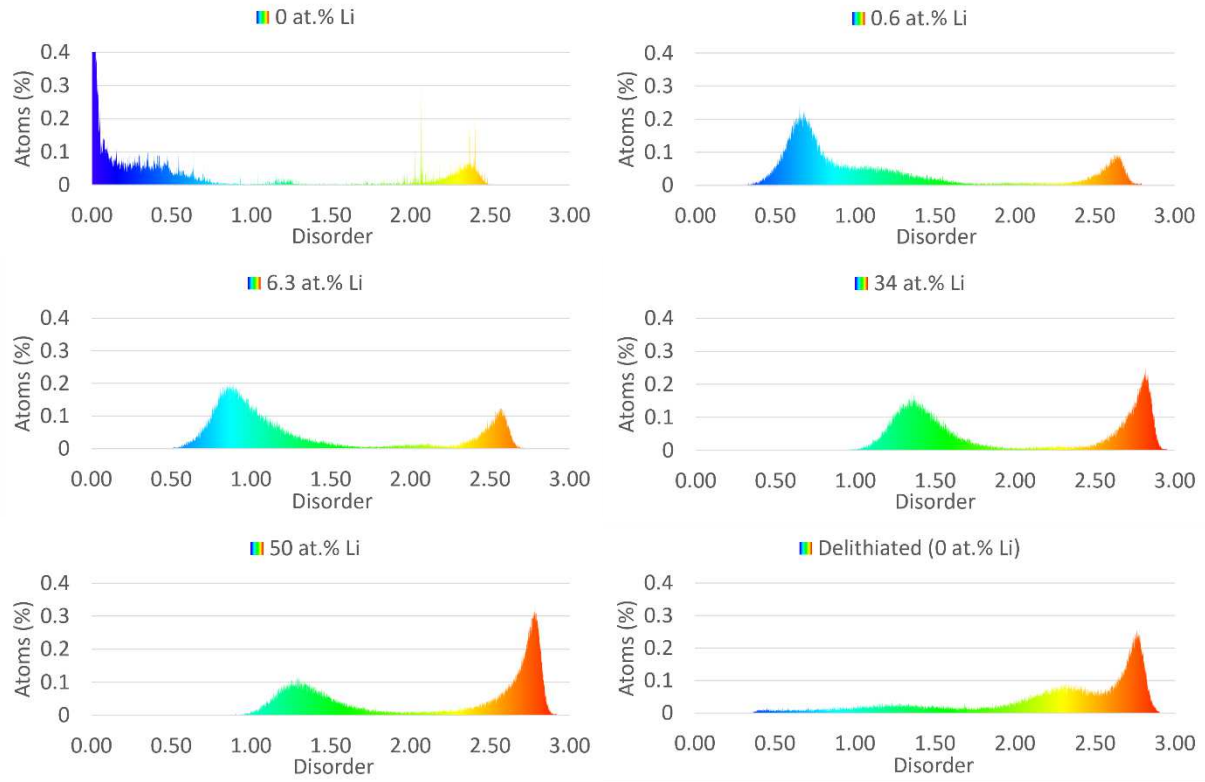

Figure 6: *Histograms showing the distribution of disorder values for core α-Al atoms at various stages of lithiation/delithiation.*

Average disorder values across the thickness of the anode for all runs are shown in **Figure 7**. For the unlithiated sample, a jagged line hovering around $\mathcal{X} \approx 0.5$ persisted throughout the anode, with a pair of twin peaks occurring at $z \approx 25$ Å corresponding to a horizontal (i.e. normal to $\vec{z}$) grain boundary. The slab-wide increase in disorder from 0-0.6 $at.\%$ Li mentioned above, is clearly visible in this figure. By 6.3 $at.\%$ Li, the average values of disorder were less constant across the

thickness, and showed a steady increase towards a maximum at the surface-core interface. This trend remained for both 9.2 and 20 $at.\%$ Li, though the latter saw a significant increase in the disorder values near the interface, coinciding with the formation of the high-disorder network. The disorder values at the interface reached their overall peak at 34 $at.\%$ Li, as the high-disorder sea formed, which also marked the point at which the difference in disorder values between the interface and core regions of the anode was the largest. From 34-50 $at.\%$ Li, average disorder values at the interface remained mostly unchanged, hovering around $\mathcal{X} \in [2.5, 2.75]$, though disorder values for bulk atoms increased making the slope towards the interface noticeably less steep. By full lithiation, average disorder values across the bulk of the anode were higher for most of $z \in [10, 27]$ Å than all preceding runs. After delithiation, disorder values near the interface dropped to $\mathcal{X} \approx 2.2$ and the trend no longer tended towards a maximum, though high disorder values persisted across the bulk region of the anode.

4 Discussion

Results from tensile samples T1,T2,T3 showed clear shifts in accumulated disorder against increases in longitudinal strain. High Cohen's d values from T1→T2→T3 suggested these shifts were large relative to the variance of the populations. Though inconclusive from the sample size, **Figure 5** suggested an approximately linear correlation between average disorder and strain for the tensile samples. The uniform increases in disorder across EBSD maps from T1→T2→T3 are in agreement with the uniform strain expected in the gauge region of a metallic tensile sample [40]. The approximately normal distributions shown in **Figure 3** and the non-skewed nature of the distributions are also both expected results for how a distribution of damage would present in strained aluminium. More extensive testing, and to higher strains, would improve insight into the working range of $\mathcal{X}$, though the results overall suggest that within $\varepsilon_{plastic} \in [0, 8.48]\%$, the disorder map serves as a promising proxy for damage in aluminium.

Reverting the plastic strain from tensile tests T1, T2, T3 to a longitudinal strain, which in fact remains $\varepsilon_l \in [0, 8.48]\%$ since $\varepsilon_{yield} \approx 0$, gives a useful domain. The maximum areawide strain for the surface-core interface across all simulation runs is 17.8%, as in **Table 4**. Assuming equal expansion along $\vec{x}$ and $\vec{y}$, which is directly observed in the spatial maps, a maximum elongation of ~8.55% occurs along the x and y axes over runs L1-D. Though this strain is biaxial, the maximum strain magnitude along a single axis is very similar for simulation run L11 and tensile test T3. Since $\mathcal{X}$ is defined mathematically and not tailored to any specific application, these results provide some confidence in the use of $\mathcal{X}$ to measure other disorder-inducing phenomena such as lithiation-induced volume expansion, within this strain limit. It is argued that the spatial maps obtained from $\mathcal{X}$ provide insight into the distribution of damage in aluminium metal, and may thus serve as a proxy for lithiation damage in simulation runs L1-D. The monotonic relationship between $\mathcal{X}$ and ε shown in **Figure 5** for both tensile tests and simulation runs, provides further confidence in this regard.

In an aluminium anode LIB, lithiation proceeds by a β-LiAl front that propagates through the anode and results in a differential volume expansion of 90-100% across this direction [4, 7, 11]. The measured expansion of 115% from simulation runs L1→L11 and the segregation of the anode into a lithiated surface and unlithiated core, supports the idea that the lithiation of an aluminium anode was justifiably simulated under the constraints of molecular dynamics. That the volume expansion was larger than expected is likely due to the use of a disordered LiAl surface phase rather than crystalline β-LiAl. It is nonetheless argued that the simulated interface between the expanded lithiated surface phase and the unexpanded α-Al core phase is comparable to interface between α-Al atoms and the β-LiAl front in a LIB anode. In particular, that which would be expected at the surface of the anode where lithiation begins and the front forms. Since the lithiation front proceeds down only once $50\ at.\%$ Li is reached [4], the simulation approximates the expansion of the aluminium anode up to and including the front's formation. The persistent expansion of the core and surface regions after delithiation is not an expected result, and is likely also due to the lack of recrystallization facilitated in the simulated timeframe. This suggests that values of $\mathcal{X}$ may be exaggerated in run D from those which would be expected in a delithiated anode.

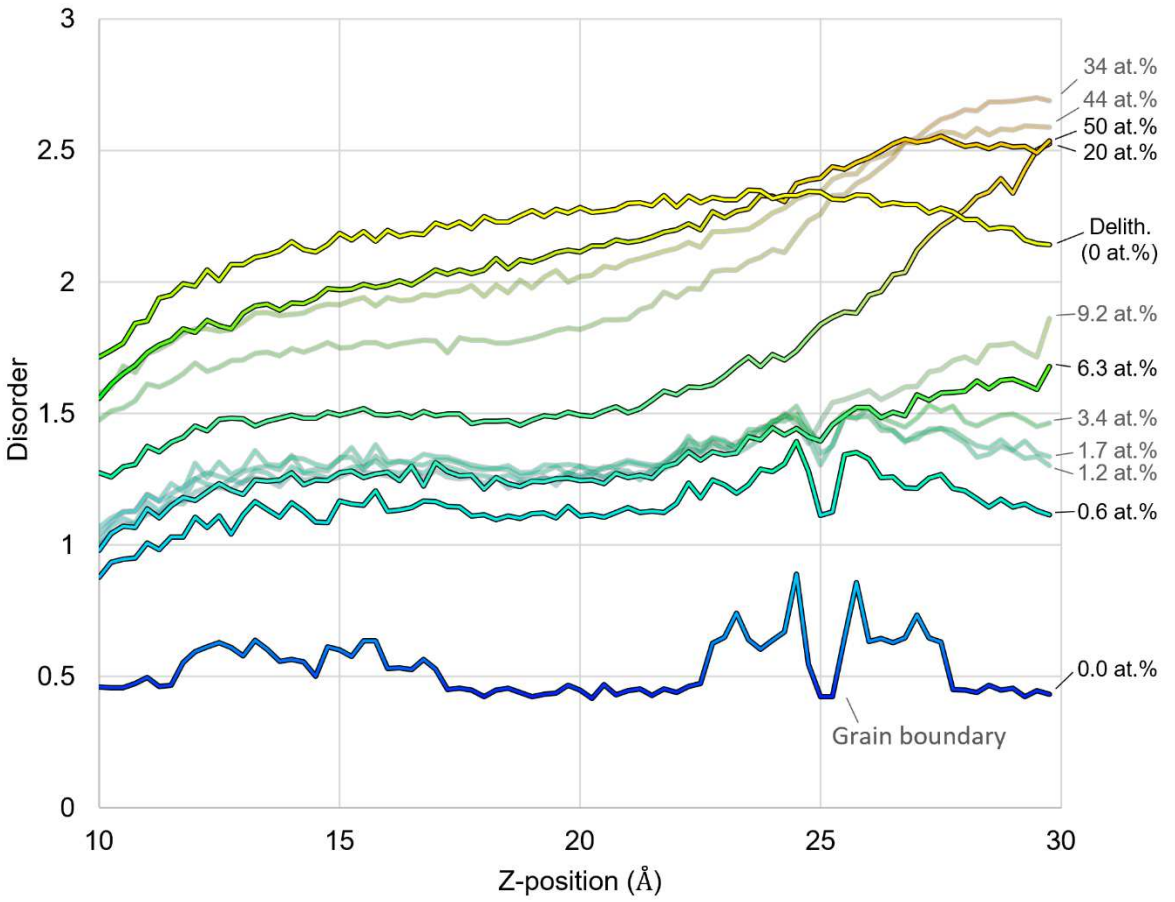

Figure 7: *Line chart showing disorder values of core α-Al atoms as a function of distance along the z axis.*

The spatial maps of disorder, such as those shown in **Figure 4**, suggest that evidence of lithiation damage begins at $\sim 1\ at.\%$ Li, as pockets of high-disorder atoms form near the lithiated surface phase. As lithiation proceeds, these pockets increase in number rather than growing, until forming into a network between 9 and $20\ at.\%$ Li. This mechanism of disorder spread is unique to the interface, and the larger pockets of disorder which later form in the bulk of the anode primarily grow rather than forming new regions, as more Li atoms are added. By the formation of the amorphous sea at $34\ at.\%$ Li, it is clear that the microstructure near the interface has been entirely destroyed. This suggests that the disorder accumulated during lithiation breaks down the crystal structure of aluminium, and that this breakdown begins at the interface, between $20\text{-}34\ at.\%$ Li. This is also the composition range over which disorder begins to propagate through the bulk of the anode, and form contrasting low- and high-disorder regions. Comparing this with the results of **Figure 7** suggests that it is at this stage in the lithiation process where significant disorder has begun to accumulate within the bulk of the anode.

Furthermore, these results suggest that disorder at the interface remains relatively constant after $34\ at.\%$ Li, though propagates throughout the rest of the anode via the aforementioned growth of the high-disorder bulk regions. Two claims are thus made. Firstly, that disorder further down the bulk of the anode seems dependent on that at the interface between the lithiated and unlithiated phases. And secondly, that disorder only appears to proceed down into the bulk of the anode once it has reached a maximum at the interface and can no longer be accommodated.

While the interface network transformed into a high-disorder sea as disorder values reach their peak, the bulk region has contrasting low- and high-disorder regions directly adjacent to one another, which remain by the time full lithiation ($50\ at.\%$ Li) has been reached. That said, average grain size had shrunk considerably by this composition, due to the incorporation of low-disorder grains into high-disorder amorphous zones. This supports previous claims that the microstructure of aluminium anodes breaks down into smaller grains after the first charge cycle [4], though support of this claim remains speculative at the angstrom-scale size of the simulation. What these results do suggest, however, is that microstructural degradation occurs even in regions of the anode which are never lithiated, but which sit nearby those which are. One might hypothesize, from these results, that high-disorder bulk regions define areas where crystallinity is weakened, and thus dislocation movement is less impeded by grain boundaries [33], though this claim cannot be directly made from the results above.

Results from the delithiated sample showcase further reductions in the size of low-disorder grains, as atoms relax from their lithiated positions and spread out into a connected, amorphous zone. Disorder appears to persist in the bulk of the delithiated anode to a greater degree than at the interface, which may suggest that stored disorder from previous charging cycles does not reliably dissipate after delithiation in aluminium anodes. Further investigations into the spatial arrangement of disorder after multiple charge cycles were performed, would however be needed to substantiate this claim.

The increase in average disorder values from the bulk region to the interface, shown in **Figure 7**, is an expected result, showing that the interface is the site of maximum disorder in the anode.

That this slope is sharper at 20 $at.\%$ Li and sharpest at 34 $at.\%$ Li as the high-disorder network and sea form, is in keeping with the results of the spatial maps. The reduction in the steepness of this slope during the later stages of lithiation (i.e. from 34-50 $at.\%$ Li) coincides with the propagation of high-disorder regions through the anode. These results also support the claim above that it is during this stage of lithiation wherein significant disorder has begun to accumulate within the bulk of the anode.

The frequency distributions in **Figure 6** suggest that a bimodal distribution of disorder exists within a lithiated anode, with low- and high-disorder proportions shrinking and growing, respectively, throughout lithiation. The shift of the left peak from $\sim$0.7 to $\sim$1.3 over the composition range 0.6-34 $at.\%$ Li, indicates that an increase in disorder values for low-disorder regions occurs during the early stages of lithiation. That no such shift occurs after 34 $at.\%$ Li supports the previous claim that the disorder values of low- and high-disorder regions do not change meaningfully after the formation of the high-disorder sea. That the right peak does not shift meaningfully from 0.6-50 $at.\%$ Li suggests that lithiation causes a transition of low-disorder atoms into high-disorder ones, rather than a steady increase. This is supported by the spatial results in the bulk of the anode, whereby adjacent high and low-disorder regions exist in clear contrast to each other without gradients between them. That this is simply a result of PTM failing to index amorphous atoms is contradicted by the decrease in disorder observed for the amorphous sea between runs L11 and D. In neither run is a grain-indexed microstructure visible, though values of disorder differ greatly between them. This would suggest that as aluminium anodes are lithiated, more and larger high-disorder regions form, but the extent of disorder in existing high-disorder regions is not significantly altered.

Several limitations need to be noted regarding the results of this study. The small number of tensile samples brings into question the degree to which the use of $\mathcal{X}$ as a proxy for damage in aluminium may be supported by samples T1-T3. Furthermore, that tensile samples underwent uniaxial strain, a volume-preserving process, does not directly support the use of $\mathcal{X}$ to model damage in expanded lithiated anodes. The angstrom-scale size of the simulation means that grains defined in the aluminium sample consisted of far fewer atoms than would be expected in actuality, which may have influenced how lithiation damage presented in the anode, and the response of aluminium atoms to the insertion of Li. Artefacts from OVITO's assignment of grain IDs to unindexed atoms led to inflated disorder values near grain boundaries which may have affected GD. Furthermore, changes in grain size and morphology between tensile samples may too have affected GD values, and could have been the reason why a correlation between GD and plastic strain was not observed, as expected from that observed between plastic strain and GOS in previous studies [31, 32, 50]. That GD fell into buckets where values remained relatively constant for several runs, suggests that the limited number of grains (18-23), poor indexing, or grain morphology and size variations may have affected the results of GD and thus $\mathcal{X}$. Lateral faces were modelled as free in the simulation to allow for in-plane volume expansion, though aluminium foil anodes are laterally constrained in actuality. Lastly, that Li atoms were inserted directly into the surface of the anode, rather than through electrochemical diffusion, that no solid-electrolyte interphase (SEI)

effects were modelled and that the lithiation front was modelled as an amorphous equivalent composition of lithium atoms, rather than a distinct β-LiAl phase, may have affected the relevance of the simulation results to the lithiation of aluminium anodes. This is especially true for run D, since atoms were not given sufficient time to recrystallize into grains.

5 Conclusions

Overall, the results of this study suggest that $\mathcal{X}$ is a promising candidate proxy for mapping damage in aluminium metal. The results of this function suggest that damage in lithiated aluminium anodes presents as a breakdown of the metal's microstructure, beginning at the Al-LiAl interface and spreading down into the bulk of the anode once a threshold has been reached. To expand upon these findings, more extensive validation on the workable domains of $\mathcal{X}$ and the connection between disorder and lithiation damage, as well as experimental studies into the effects of high-disorder regions on dislocation mobility, may build on the results of this study and provide further insight into the degradation of aluminium anodes in lithium-ion batteries.

Acknowledgements

Recognition is due to the labs and facilities at the University of Cape Town (UCT) for their contributions to this project. Aluminium samples were machined into tensile samples by the UCT Mechanical Engineering Workshop. EBSD maps were obtained using resources of the UCT Electron Microscopy Unit, and LAMMPS computations for the lithiation simulation were performed using facilities provided by the UCT ICTS High-Performance Computing Team. This study was supported solely by internal institution funding. The authors gratefully acknowledge financial support for this research from the Centre for Materials Engineering at UCT.

Conflict of Interest

The authors declare no conflict of interest.

CRediT Statement

Mikael Christodoulides: Conceptualization, Methodology, Software, Validation, Formal analysis, Investigation, Writing - Original Draft, Visualization. **Thorsten Becker**: Methodology**,** Supervision, Resources, Writing - Review & Editing. **Gerhard Venter**: Software, Supervision, Resources, Writing - Review & Editing.

Data Access

Data that support the findings of this study are available from the corresponding author, M.C., upon reasonable request. All code used for data processing and analysis is hosted on GitHub at the following url: https://github.com/Mikael-DT-Christodoulides/INVESTIGATING-LITHIATION-DAMAGE-IN-AL-METAL-ANODES.

References

[1] M. Nieradko, L. Eskandarian, and O. A. Semenikhin, "Aluminum anodes coated with polymer electrolyte show improved reversibility and cycling ability in Li-Ion batteries," *Electrochim Acta,* vol. 327, Dec 2019, doi: 10.1016/j.electacta.2019.135023.

[2] B. S. Qin *et al.*, "Enabling Reversible (De)Lithiation of Aluminum by using Bis(fluorosulfonyl)imide-Based Electrolytes," *Chemsuschem,* vol. 12, no. 1, pp. 208–212, Jan 2019, doi: 10.1002/cssc.201801806.

[3] B. S. Qin, A. Varzi, and S. Passerini, "Revisiting the Electrochemical Lithiation Mechanism of Aluminum and the Role of Li-rich Phases (LiAl) on Capacity Fading," *Chemsuschem,* vol. 12, no. 12, Jun 2019, doi: 10.1002/cssc.201901507.

[4] T. Y. Zheng and S. T. Boles, "Lithium aluminum alloy anodes in Li-ion rechargeable batteries: past developments, recent progress, and future prospects," *Prog Energy,* vol. 5, no. 3, Jul 2023, doi: 10.1088/2516-1083/acd101.

[5] H. Wang *et al.*, "The progress on aluminum-based anode materials for lithium-ion batteries," *Journal of Materials Chemistry A,* vol. 8, no. 48, pp. 25649–25662, 2020, doi: 10.1039/d0ta09762d.

[6] S. S. Sharma, P. J. Crowley, and A. Manthiram, "Aluminum–Silicon Alloy Foils as Low-Cost, Environmentally Friendly Anodes for Lithium-Ion Batteries," *American Chemical Society Sustainable Chemistry & Engineering,* vol. 9, no. 43, pp. 14515–14524, 2021, doi: 10.1021/acssuschemeng.1c05168.

[7] H. Li *et al.*, "Circumventing huge volume strain in alloy anodes of lithium batteries," *Nature Communications,* vol. 11, no. 1, p. 1584, Apr 2020, doi: 10.1038/s41467-020-15452-0.

[8] M. H. Tahmasebi, D. Kramer, R. Mönig, and S. T. Boles, "Insights into Phase Transformations and Degradation Mechanisms in Aluminum Anodes for Lithium-Ion Batteries," *Journal of The Electrochemical Society,* vol. 166, no. 3, p. A5001, 2019, doi: 10.1149/2.0011903jes.

[9] L. L. Yang *et al.*, "Grain boundary density matters in lithiation performances of aluminum foil anode for lithium ion batteries," *Materials Today Communications,* vol. 37, Dec 2023, doi: 10.1016/j.mtcomm.2023.107179.

[10] T. Zheng, D. Kramer, R. Mönig, and S. T. Boles, "Aluminum Foil Anodes for Li-Ion Rechargeable Batteries: the Role of Li Solubility within β-LiAl," *American Chemical Society Sustainable Chemistry & Engineering,* vol. 10, no. 10, pp. 3203–3210, 2022, doi: 10.1021/acssuschemeng.1c07242.

[11] X. Zhang *et al.*, "Solid electrolyte interphase layer induced electrochemical behavior diversity of aluminum foil anode for lithium ion batteries," *Solid State Ionics,* vol. 387, Dec 2022, doi: 10.1016/j.ssi.2022.116081.

[12] N. Hudak and D. Huber, "Nanostructured Lithium-Aluminum Alloy Electrodes for Lithium-Ion Batteries," *Electrochemical Society Transactions,* vol. 33, no. 24, 2011, doi: 10.1149/1.3557706.

[13] T. S. Huang and J. O. Brittain, "The Mechanical-Behavior of Beta-Lial," *Mater Sci Eng,* vol. 93, pp. 93–97, Sep 1987, doi: 10.1016/0025-5416(87)90415-0.

[14] G. Oltean, C. W. Tai, K. Edström, and L. Nyholm, "On the origin of the capacity fading for aluminium negative electrodes in Li-ion batteries," *Journal of Power Sources,* vol. 269, pp. 266–273, Dec 2014, doi: 10.1016/j.jpowsour.2014.06.118.

[15] J. Y. Huang *et al.*, "In Situ Observation of the Electrochemical Lithiation of a Single SnO2 Nanowire Electrode," *Science,* vol. 330, no. 6010, pp. 1515–1520, 2010, doi: 10.1126/science.1195628.

[16] P. Novák, J. C. Panitz, F. Joho, M. Lanz, R. Imhof, and M. Coluccia, "Advanced in situ methods for the characterization of practical electrodes in lithium-ion batteries," *Journal of Power Sources,* vol. 90, no. 1, pp. 52–58, Sep 2000, doi: 10.1016/S0378-7753(00)00447-X.

[17] A. Zaboli, H. Raissi, H. Hashemzadeh, and F. Farzad, "Toward efficient electrodes for a high-performance fast-charge Li-ion battery: molecular dynamics simulation and DFT calculations," *Physical Chemistry Chemical Physics,* vol. 25, no. 35, pp. 23937–23953, 2023, doi: 10.1039/d2cp06020e.

[18] D. E. Galvez-Aranda, V. Ponce, and J. M. Seminario, "Molecular dynamics simulations of the first charge of a Li-ion-Si-anode nanobattery," *Journal of Molecular Modeling,* vol. 23, no. 4, Apr 2017, doi: 10.1007/s00894-017-3283-2.

[19] H. Y. Yang, R. Z. Chen, S. H. Fu, S. X. Mo, Y. L. Chen, and J. F. Cao, "Atomic-Scale Modulation of Lithium Metal Electrode Interfaces by Monolayer Graphene: A Molecular Dynamics Study," *Materials,* vol. 18, no. 21, Oct 2025, doi: 10.3390/ma18214925.

[20] F. Ospina-Acevedo, N. Guo, and P. B. Balbuena, "Lithium oxidation and electrolyte decomposition at Li-metal/liquid electrolyte interfaces," *Journal of Materials Chemistry A,* vol. 8, no. 33, pp. 17036–17055, 2020, doi: 10.1039/d0ta05132b.

[21] A. P. Thompson *et al.*, "LAMMPS - a flexible simulation tool for particle-based materials modeling at the atomic, meso, and continuum scales," *Computer Physics Communications,* vol. 271, p. 108171, Feb 2022, doi: 10.1016/j.cpc.2021.108171.

[22] H. Y. Wang, X. Ji, C. Chen, K. Xu, and L. Miao, "Lithium diffusion in silicon and induced structure disorder: A molecular dynamics study," *American Institute of Physics Advances,* vol. 3, no. 11, Nov 2013, doi: 10.1063/1.4829440.

[23] S. Wang *et al.*, "Stable aluminum metal anodes with high ionic conductivity and high aluminophilic site," *Chemical Engineering Journal,* vol. 494, p. 153194, Aug 2024, doi: 10.1016/j.cej.2024.153194.

[24] T. J. Ruggles, W. G. Gilliland, D. T. Fullwood, and J. Kacher, "An overview of HR-EBSD techniques for mapping local stress and dislocations in crystalline materials at sub-micron resolution," *Progress in Materials Science,* vol. 157, p. 101585, Mar 2026, doi: 10.1016/j.pmatsci.2025.101585.

[25] G. T. Gray III, V. Livescu, and E. K. Cerreta, "Defect and damage evolution quantification in dynamically-deformed metals using orientation-imaging microscopy," in *Materials Science Forum*, 2010, vol. 654: Trans Tech Publ, pp. 2297–2302.

[26] W. Wciślik and S. Lipiec, "Voids Development in Metals: Numerical Modelling," *Materials,* vol. 16, no. 14, p. 4998, 2023, doi: 10.3390/ma16144998.

[27] B. Luccioni, S. Oller, and R. Danesi, "Coupled plastic-damaged model," *Computer Methods in Applied Mechanics and Engineering,* vol. 129, no. 1, pp. 81–89, Jan 1996, doi: 10.1016/0045-7825(95)00887-X.

[28] A. Harte, M. Atkinson, M. Preuss, and J. Q. da Fonseca, "A statistical study of the relationship between plastic strain and lattice misorientation on the surface of a deformed Ni-based superalloy," *Acta Materialia,* vol. 195, pp. 555–570, Aug 2020, doi: 10.1016/j.actamat.2020.05.029.

[29] L. Brewer, M. Othon, L. Young, and T. Angeliu, "Misorientation mapping for visualization of plastic deformation via electron back-scattered diffraction," *Microscopy and Microanalysis,* vol. 12, no. 1, pp. 85–91, 2006.
[30] M. Kamaya and N. Maekawa, "A procedure to obtain correlation curve between local misorientation and plastic strain," *Materials Characterization,* vol. 198, Apr 2023, doi: 10.1016/j.matchar.2023.112725.
[31] M. Kamaya, A. J. Wilkinson, and J. M. Titchmarsh, "Measurement of plastic strain of polycrystalline material by electron backscatter diffraction," *Nuclear Engineering and Design,* vol. 235, no. 6, pp. 713–725, Mar 2005, doi: 10.1016/j.nucengdes.2004.11.006.
[32] M. Kamaya, A. J. Wilkinson, and J. M. Titchmarsh, "Quantification of plastic strain of stainless steel and nickel alloy by electron backscatter diffraction," *Acta Materialia,* vol. 54, no. 2, pp. 539–548, Jan 2006, doi: 10.1016/j.actamat.2005.08.046.
[33] M. Kamaya, "Assessment of local deformation using EBSD: Quantification of local damage at grain boundaries," *Materials Characterization,* vol. 66, pp. 56–67, 2012.
[34] U. Müller, *Symmetry relationships between crystal structures: applications of crystallographic group theory in crystal chemistry*. OUP Oxford, 2013.
[35] V. Senashov, "Applications of group theory in crystallography," *IOP Conference Series: Materials Science and Engineering,* vol. 1230, p. 012018, 2022, doi: 10.1088/1757-899X/1230/1/012018.
[36] P. H. Butler, *Point group symmetry applications: methods and tables*. Springer Science & Business Media, 2012.
[37] C. C. Pinter, *A book of abstract algebra*. Courier Corporation, 2010.
[38] J. H. Conway, H. Burgiel, and C. Goodman-Strauss, *The symmetries of things*. CRC Press, 2016.
[39] D. Q. Huynh, "Metrics for 3D Rotations: Comparison and Analysis," *Journal of Mathematical Imaging and Vision,* vol. 35, no. 2, pp. 155–164, Oct 2009, doi: 10.1007/s10851-009-0161-2.
[40] G. E. Dieter and D. Bacon, *Mechanical metallurgy*. McGraw-hill, New York, 1976.
[41] *Standard Test Methods for Tension Testing of Metallic Materials ASTM E8/E8M*, ASTM, 2025.
[42] F. Bachmann, R. Hielscher, and H. Schaeben, "Texture Analysis with MTEX – Free and Open Source Software Toolbox," *Solid State Phenomena,* vol. 160, pp. 63–68, 2010, doi: 10.4028/www.scientific.net/SSP.160.63.
[43] P. Hirel, "Atomsk: A tool for manipulating and converting atomic data files," *Computer Physics Communications,* vol. 197, pp. 212–219, Dec 2015, doi: 10.1016/j.cpc.2015.07.012.
[44] S. Roy, A. Dutta, and N. Chakraborti, "A novel method of determining interatomic potential for Al and Al-Li alloys and studying strength of Al-AlLi interphase using evolutionary algorithms," *Computational Materials Science,* vol. 190, Apr 2021, doi: 10.1016/j.commatsci.2020.110258.
[45] A. Stukowski, "Visualization and analysis of atomistic simulation data with OVITO–the Open Visualization Tool," *Modelling and Simulation in Materials Science and Engineering,* vol. 18, no. 1, p. 015012, 2010.
[46] P. M. Larsen, S. Schmidt, and J. Schiøtz, "Robust structural identification via polyhedral template matching," *Modelling and Simulation in Materials Science and Engineering,* vol. 24, no. 5, p. 055007, 2016.

[47] C. R. Harris *et al.*, "Array programming with NumPy," *Nature,* vol. 585, no. 7825, pp. 357–362, 2020.
[48] P. Virtanen *et al.*, "SciPy 1.0: fundamental algorithms for scientific computing in Python," *Nature Methods,* vol. 17, no. 3, pp. 261–272, 2020.
[49] J. A. Dean and N. A. Lange, *Lange's handbook of chemistry*, 15th ed. (Handbook of chemistry.). New York: McGraw-Hill, 1999.
[50] R. R. Shen and P. Efsing, "Overcoming the drawbacks of plastic strain estimation based on KAM," *Ultramicroscopy,* vol. 184, pp. 156–163, Jan 2018, doi: 10.1016/j.ultramic.2017.08.013.

6 Appendix

A Theorems and proofs

Lemma 1: Disorder is a well-defined map, i.e.

$$p_1 = p_2 \Longrightarrow \mathcal{X}(p_1) = \mathcal{X}(p_2) \text{ for any unit cells } p_1, p_2$$

Proof: This follows plainly from definition. Since $p_1 = p_2$, they share orientations and positions, and thus local distortions and offsets. Since GD is a constant, $\mathcal{X}(p_1) = \mathcal{X}(p_2)$. ■

Lemma 2: The relation $\sim_G$ on a set of unit cells X is an equivalence relation.

Proof: For any $p \in X$, $p \sim_G p$ since the properties of our chain $p = p_0 = p_n = p$ are vacuously true by the fact that p_{i+1} does not exist. Furthermore, given $p, q \in X$ such that $p \sim_G q$, we have that there exists a chain $p = p_0, p_1, \dots, p_n = q$ with $p_{i+1} \in N(p_i)$ and $\omega(\phi_{p_i}, \phi_{p_{i+1}}) \leq 5°$. We seek to prove both of these properties are symmetric. If $p_{i+1} \in N(p_i)$, then $\left|\overrightarrow{x_{p_i}} - \overrightarrow{x_{p_{i+1}}}\right| \leq \sqrt{3} \Longrightarrow \left|\overrightarrow{x_{p_{i+1}}} - \overrightarrow{x_{p_i}}\right| \leq \sqrt{3} \Longrightarrow p_i \in N(p_{i+1})$. Furthermore, $\omega(\phi_{p_i}, \phi_{p_{i+1}}) = \omega(\phi_{p_{i+1}}, \phi_{p_i}) \leq 5°$ since ω is symmetric (see **Theorem 3** below). Thus, there exists a chain $q = p_0, p_1, \dots, p_n = p$ with $p_{i+1} \in N(p_i)$ and $\omega(\phi_{p_{i+1}}, \phi_{p_i}) \leq 5°$ and so $q \sim_G p$. Finally, take some $p, q, r \in X$ such that $p \sim_G q, q \sim_G r$. We seek $p \sim_G r$. Clearly a valid chain exists from p to q and q to r, and the result follows plainly from this fact since q is a member of both chains. Thus, $\sim_G$ is an equivalence relation. ■

Lemma 3: $\chi(p) - \lambda(p) = \frac{1}{|N(p) \cap G|} \sum_{p' \in N(p) \cap G} \omega(\phi_p, \phi_{p'})$ for $\alpha = 1$.

Proof: We begin by noting $\mathcal{A}_p = N(p) \backslash G$ and so, too, $N(p) = (N(p) \cap G) \cup \mathcal{A}_p$. For simplicity, denote $|\mathcal{A}_p| = y$ and $|N(p) \cap G| = x$ and so $|N(p)| = |N(p) \cap G| + |\mathcal{A}_p| = x + y$, since $\mathcal{A}_p$ and $N(p) \cap G$ are disjoint. From here, note

$$\chi(p) = \frac{1}{|N(p)|} \sum_{q \in N(p)} \omega(\phi_p, \phi_q)$$
$$= \frac{1}{x+y} \left(\sum_{q \in N(p) \cap G} \omega(\phi_p, \phi_q) + \sum_{q \in \mathcal{A}_p} \omega(\phi_p, \phi_q) \right)$$
$$= \frac{x}{x} \cdot \frac{1}{x+y} \left(\sum_{q \in N(p) \cap G} \omega(\phi_p, \phi_q) + \sum_{q \in \mathcal{A}_p} \omega(\phi_p, \phi_q) \right)$$

and further that

$$\lambda(p) = (1) \left[\frac{-|\mathcal{A}_p| \sum_{q \in N(p) \cap G} \omega(\phi_p, \phi_q)}{|N(p)||N(p) \cap G|} + \frac{\sum_{q \in \mathcal{A}_p} \omega(\phi_p, \phi_q)}{|N(p)|} \right]$$
$$= \left[\frac{-y \sum_{q \in N(p) \cap G} \omega(\phi_p, \phi_q)}{(x+y)(x)} + \frac{\sum_{q \in \mathcal{A}_p} \omega(\phi_p, \phi_q)}{(x+y)} \right]$$
$$= \left[\frac{-y \sum_{q \in N(p) \cap G} \omega(\phi_p, \phi_q)}{x(x+y)} + \frac{x \sum_{q \in \mathcal{A}_p} \omega(\phi_p, \phi_q)}{x(x+y)} \right]$$

thus, altogether we have

$$\chi(p) - \lambda(p)$$
$$= \frac{x\left(\sum_{q \in N(p) \cap G} \omega(\phi_p, \phi_q) + \sum_{q \in \mathcal{A}_p} \omega(\phi_p, \phi_q) \right)}{x(x+y)} - \left[\frac{-y \sum_{q \in N(p) \cap G} \omega(\phi_p, \phi_q)}{x(x+y)} + \frac{x \sum_{q \in \mathcal{A}_p} \omega(\phi_p, \phi_q)}{x(x+y)} \right]$$

$$= \frac{x\sum_{q\in N(p)\cap G}\omega(\phi_p,\phi_q)}{x(x+y)} + \frac{x\sum_{q\in \mathcal{A}_p}\omega(\phi_p,\phi_q)}{x(x+y)} + \frac{y\sum_{q\in N(p)\cap G}\omega(\phi_p,\phi_q)}{x(x+y)} - \frac{x\sum_{q\in \mathcal{A}_p}\omega(\phi_p,\phi_q)}{x(x+y)}$$

$$= \frac{\left(\sum_{q\in N(p)\cap G}\omega(\phi_p,\phi_q)\right)(x+y)}{x(x+y)} = \frac{\sum_{q\in N(p)\cap G}\omega(\phi_p,\phi_q)}{|N(p)\cap G|}$$

as desired. ■

Lemma 4: $\forall \phi_1, \phi_2 \in SO(3)/O,\ \ \omega(\phi_1,\phi_2) \geq 0°$

Proof: By definition, distortion is given as $\omega(\phi_1,\phi_2) = \min\{\arccos\left(\frac{\mathrm{Tr}\,(x_1^{-1}x_2)-1}{2}\right) : x_1 \in \phi_1, x_2 \in \phi_2\}$, and for any $x_1 \in \phi_1, x_2 \in \phi_2$, we note that $\mathrm{Tr}(x_1^{-1}x_2) \in \mathbb{R}$. Further, since $\arccos(\mathbb{R}) = [0,180]°$, the set for which we take the minimum is a subset of this image, i.e. $[0,180]°$. Altogether,

$$\omega(\phi_1,\phi_2) = \min\left\{\arccos\left(\frac{\mathrm{Tr}\,(x_1^{-1}x_2)-1}{2}\right) : x_1 \in \phi_1, x_2 \in \phi_2\right\} \geq \min[0,180]° = 0°$$

as desired. ■

Theorem 1: If ~ is a relation defined as

$g_1 \sim g_2 \Leftrightarrow \exists o \in O\ st.\ g_2 o = g_1$, then

a) ~ is an equivalence relation
b) the equivalence classes of ~ are the left cosets of O in SO(3).

Proof: We prove a) and b) sequentially below.

a) Since O is a subgroup of $SO(3)$, we have $I_3 \in O$, thus for any $g \in SO(3)$, we have $gI_3 = g \Rightarrow g \sim g$ so reflexivity is obtained. Further, given some $g, h \in SO(3)$ such that $g \sim h$, we know $\exists o \in O$ st. $ho = g$, and so by basic group multiplication laws, $ho = g \Rightarrow ho(o^{-1}) = go^{-1} \Longrightarrow hI_3 = h = go^{-1}$ meaning $h \sim g$ since $o^{-1} \in O$. Finally, given $a, b, c \in SO(3)$ where $a \sim b, b \sim c$, we have $\exists o_1, o_2 \in O$ with $bo_1 = a, co_2 = b$, and thus $bo_1 = (co_2)o_1 = c(o_2 o_1) = a$ and clearly $o_2 o_1 \in O$ by closure, thus $a \sim c$. Thus, ~ is an equivalence relation as desired.
b) This follows clearly from definition. Take some arbitrary $g \in SO(3)$, then for any $x \in [g]$, we have that $x \sim g \Longrightarrow \exists o_1 \in O$ with $go_1 = x$ but then $x \in gO$. Also, for any $x \in gO$, we have that $\exists o_2 \in O$ such that $x = go_2$ but then by definition $x \sim g$ so $x \in [g]$. Thus, $[g] = gO$ as desired. ■

Theorem 2: If global distortion is one, then no disorder is present, i.e.

$$GD = 1 \Rightarrow \mathcal{X}(p) = 0 \text{ for any unit cell } p$$

Proof: We have that $GD = 1$, thus $\sum_{G\in\mathcal{G}}\sum_{p\in G}\omega(\phi_G,\phi_p) = 0$. As such, from **Lemma 4**, we have that $\omega(\phi_G,\phi_p) = 0$ for any $G \in \mathcal{G}, p \in G$. Thus, $\forall p \in G$ there exist $x_1 \in \phi_G, x_2 \in \phi_p$ such that $\arccos\left(\frac{\mathrm{Tr}(x_1^{-1}x_2)-1}{2}\right) = 0 \Rightarrow \mathrm{Tr}(x_1^{-1}x_2) = 3$ and thus $x_1^{-1}x_2 = I_3$ since $x_1^{-1}x_2 \in SO(3)$ by

closure of the group. Therefore, we must have $x_1 = x_2 \implies \phi_G = \phi_p$ and more generally $\phi_{p_1} = \phi_{p_2}$ for arbitrary $p_1, p_2 \in G$. Thus, note $N(p) \cap G \subseteq G$ implies that $\sum_{p' \in N(p) \cap G} \omega(\phi_p, \phi_{p'}) \leq \sum_{p' \in G} \omega(\phi_p, \phi_{p'}) = 0$, again by **Lemma 4**. Lastly, using **Lemma 3**, obtain

$$\mathcal{X}(p) = \log\left[\left(\chi(p) - \lambda(p)\right) GD + 1\right]$$

$$= \log\left[\frac{1}{|N(p) \cap G|} \sum_{p' \in N(p) \cap G} \omega(\phi_p, \phi_{p'}) + 1\right]$$

$$= \log[0 + 1] = 0$$

as desired. ■

Theorem 3: Given a set of orientations $\mathcal{O}$, then $(\mathcal{O}, \omega)$ is a metric space.

Proof: We prove the three properties of a metric sequentially. First, given some $\phi_1 \in \mathcal{O}$, we have that $\omega(\phi_1, \phi_1) = 0$ since for any $x \in \phi_1, \frac{\mathrm{Tr}(x^{-1}x)-1}{2} = \frac{\mathrm{Tr}(I_3)-1}{2} = \frac{3-1}{2} = 1$ and note $\arccos 1 = 0$. The converse is given by **Theorem 2** above. Next, take some $\phi_1, \phi_2 \in \mathcal{O}$ and some $x_1 \in \phi_1, x_2 \in \phi_2$ such that $\omega(\phi_1, \phi_2) = \arccos\frac{\mathrm{Tr}(x_1^{-1}x_2)-1}{2}$. Now note that $\mathrm{Tr}(A) = \mathrm{Tr}(A^{\mathrm{T}}) = \mathrm{Tr}(A^{-1})$ for any $A \in SO(3)$ by properties of the trace. As such, we obtain $\omega(\phi_1, \phi_2) = \arccos\frac{\mathrm{Tr}(x_1^{-1}x_2)-1}{2} = \arccos\frac{\mathrm{Tr}(x_2^{-1}x_1)-1}{2} \geq \omega(\phi_2, \phi_1)$ since $\arccos\frac{\mathrm{Tr}(x_2^{-1}x_1)-1}{2} \in \left\{\arccos\frac{\mathrm{Tr}(x^{-1}y)-1}{2} \mid x \in \phi_2, y \in \phi_1\right\}$ for which the minimum is $\omega(\phi_2, \phi_1)$. By a similar argument, $\omega(\phi_1, \phi_2) \leq \omega(\phi_2, \phi_1)$, and by antisymmetry of $\leq$ obtain $\omega(\phi_1, \phi_2) = \omega(\phi_2, \phi_1)$ as desired. Finally, to prove the triangle inequality, we use a result proven by D.Q. Huynh in a previous paper [39], namely that $\theta(x, y) = \arccos\frac{\mathrm{Tr}(x^{-1}y)-1}{2}$ is a metric on $SO(3)$. In addition, though **Definition 4** allows for a minimum pair to be found by cycling through both orientations, it may be shown for any ϕ_1, ϕ_2 and fixed $x \in \phi_1$ that there exists some $y \in \phi_2$ such that $\theta(x, y) = \omega(\phi_1, \phi_2)$. Thus, for any $\phi_1, \phi_2, \phi_3 \in \mathcal{O}$, take some fixed $x \in \phi_1$ and corresponding $y \in \phi_2$ st. $\omega(\phi_1, \phi_2) = \arccos\frac{\mathrm{Tr}(x^{-1}y)-1}{2} = \theta(x, y)$ and then with this $y \in \phi_2$ the corresponding $z \in \phi_3$ such that $\omega(\phi_2, \phi_3) = \arccos\frac{\mathrm{Tr}(y^{-1}z)-1}{2} = \theta(y, z)$. Also note $\omega(\phi_1, \phi_3) = \min\{\theta(a, b) \mid a \in \phi_1, b \in \phi_3\}$, and so $\omega(\phi_1, \phi_3) \leq \theta(x, z)$. Thus, by the triangle inequality of θ, obtain $\omega(\phi_1, \phi_3) \leq \theta(x, z) \leq \theta(x, y) + \theta(y, z) = \omega(\phi_1, \phi_2) + \omega(\phi_2, \phi_3)$, as desired. ■

Theorem 4: Given a set of orientations $\mathcal{O}$, then ω induces a topology τ on $\mathcal{O}$.

Proof: This follows directly from **Theorem 3** and a general result in metric spaces. Given any metric space (A, d), then d induces a topology composed of the open sets in $\mathcal{P}(A)$ under d. As such, the set τ given as the set of open sets in $(\mathcal{O}, \omega)$, is a topology. ■